Mon. Not. R. Astron. Soc. **000**, 1–17 (2013) Printed 13 May 2014 (MN LATEX style file v2.2)

An updated analytic model for the attenuation by the intergalactic medium

Akio K. Inoue[1⋆], Ikkoh Shimizu,[1,2], Ikuru Iwata[3], and Masayuki Tanaka[4]

[1] *College of General Education, Osaka Sangyo University, 3-1-1, Nakagaito, Daito, Osaka 574-8530, Japan*
[2] *Department of Astronomy, The University of Tokyo, 7-3-1 Hongo, Tokyo 113-0033, Japan*
[3] *Subaru Telescope, National Astronomical Observatory of Japan, 650 North A'ohoku Place Hilo, HI 96720, USA*
[4] *National Astronomical Observatory of Japan, 2-21-1, Osawa, Mitaka, Tokyo 181-8588, Japan*

ABSTRACT

We present an updated version of the so-called Madau model for the attenuation by the intergalactic neutral hydrogen against the radiation from distant objects. First, we derive a distribution function of the intergalactic absorbers from the latest observational statistics of the Lyα forest, Lyman limit systems, and damped Lyα systems. The distribution function excellently reproduces the observed redshift evolutions of the Lyα depression and of the mean-free-path of the Lyman continuum simultaneously. Then, we derive a set of the analytic functions which describe the mean intergalactic attenuation curve for objects at $z > 0.5$. The new model predicts less (or more) Lyα attenuation for $z \simeq 3$–5 ($z > 6$) sources through usual broad-band filters relative to the original Madau model. This may cause a systematic difference in the photometric redshift estimates, which is, however, still as small as about 0.05. Finally, we find a more than 0.5 mag overestimation of the Lyman continuum attenuation in the original Madau model at $z > 3$, which causes a significant overcorrection against direct observations of the Lyman continuum of galaxies.

Key words: cosmology: observations — galaxies: high-redshift — intergalactic medium

1 INTRODUCTION

Radiation from cosmological sources is absorbed by neutral hydrogen left in the intergalactic medium (IGM) even after the cosmic reionization (e.g. Gunn & Peterson 1965). This intergalactic neutral hydrogen probably traces 'cosmic web' produced by the gravity of the dark matter (e.g. Rauch 1998). Along an observer's line-of-sight piercing the cosmic web, there appear to be numerous discrete systems composed of the intergalactic neutral hydrogen producing a number of absorption lines in the spectra of distant sources. These systems are divided into the Lyα forest (LAF; $\log_{10}(N_{\rm HI}/{\rm cm}^{-2}) < 17.2$), Lyman limit systems (LLSs; $17.2 \leqslant \log_{10}(N_{\rm HI}/{\rm cm}^{-2}) < 20.3$) and damped Ly$\alpha$ systems (DLAs; $\log_{10}(N_{\rm HI}/{\rm cm}^{-2}) \geqslant 20.3$), depending on the column density of the neutral hydrogen along the line-of-sight (e.g. Rauch 1998).

The intergalactic absorption is routinely found in the spectra of objects at a cosmological distance and this feature is utilized as a tool to select high-z objects only by photometric data: the so-called drop-out technique (e.g. Steidel et al. 1995; Madau et al. 1996). To put it another way, we must always correct the spectra of cosmological sources for this absorption in order to know the intrinsic ones. Therefore, an accurate model of this absorption is quite useful as a standard tool for observational cosmology.

After several models for this purpose were presented (e.g., Møller & Jakobsen 1990; Zuo 1993; Yoshii & Peterson 1994), Madau (1995) (hereafter M95) appeared and became the most popular because of the convenient analytic functions. However, the heart of the model, i.e. the statistics of the LAF, LLSs, and DLAs, has been updated largely by observations in the last two decades since M95. In fact, there are several papers adopting such updated statistics (Bershady et al. 1999; Meiksin 2006; Tepper-García & Fritze 2008; Inoue & Iwata 2008). Nevertheless, people still adhere to M95, except for a few innovative authors (e.g. Harrison et al. 2011; Overzier et al. 2013). This adherence may be due to the simplicity and convenience of the

⋆ E-mail: akinoue@las.osaka-sandai.ac.jp

analytic functions in M95. Here, in this paper, we intend to present a user-friendly analytic function conforming to updated statistics.

In the next section, we introduce the heart of the modeling: the distribution function of the intergalactic absorbers derived from the latest observational data of the LAF, LLSs, and DLAs. Then, we show the updated mean transmission function and compare it with the latest observations of the Lyα transmission and the mean-free-path of Lyman limit photons in section 3. In section 4, we present new analytic formulae of the intergalactic attenuation. Finally, we quantify the difference of the attenuation magnitudes through some broad-band filters between the M95 model and ours and discuss the effect on the drop-out technique and the photometric redshift estimation in section 5. We do not need to assume any specific cosmological model in this paper, except for sections 2.1 and 3.2, where we assume $\Omega_{\rm M} = 0.3$, $\Omega_\Lambda = 0.7$, and $H_0 = 70$ km s^{-1} Mpc^{-1}. Therefore, the analytic functions presented in section 4 can be used directly in any cosmological models.

2 DISTRIBUTION FUNCTION OF INTERGALACTIC ABSORBERS

The mean optical depth at the observed wavelength $\lambda_{\rm obs}$ along a line-of-sight, where we assume that absorbers distribute randomly[1], towards a source at $z_{\rm S}$ is (e.g. Paresce et al. 1980; Madau 1995)

$$\langle \tau^{\rm IGM}_{\lambda_{\rm obs}}(z_{\rm S}) \rangle = \int_0^{z_{\rm S}} \int_0^{\infty} \frac{\partial^2 n}{\partial z \partial N_{\rm HI}} (1 - e^{-\tau_{\rm abs}}) dN_{\rm HI} dz \,, \tag{1}$$

where $\partial^2 n / \partial z / \partial N_{\rm HI}$ is the distribution function of the intergalactic absorbers and $\tau_{\rm abs} = \sigma^{\rm HI}_{\lambda_{\rm abs}} N_{\rm HI}$ is the optical depth of an absorber with the H I column density $N_{\rm HI}$ at the redshift z and the H I cross section $\sigma^{\rm HI}_{\lambda_{\rm abs}}$, which includes an assumed line profile for Lyman series absorption, at the wavelength in the absorber's rest-frame $\lambda_{\rm abs} = \lambda_{\rm obs}/(1+z)$. By specifying the distribution function, we can integrate equation (1) analytically if possible or numerically. Thus, an appropriate distribution function is essential for the model of the intergalactic absorption.

M95 assumed the following function:

$$\frac{\partial^2 n}{\partial z \partial N_{\rm HI}} = \begin{cases} 2.4 \times 10^7 N_{\rm HI}^{-1.5} (1+z)^{2.46} & (2 \times 10^{12} < N_{\rm HI}/{\rm cm}^{-2} < 1.59 \times 10^{17}) \\ 1.9 \times 10^8 N_{\rm HI}^{-1.5} (1+z)^{0.68} & (1.59 \times 10^{17} < N_{\rm HI}/{\rm cm}^{-2} < 2 \times 10^{20}) \end{cases} , \tag{2}$$

where the column density distribution is assumed to be a single power-law with the index of -1.5 but the redshift distribution is divided into two parts: one for the LAF and the other for LLSs. Since the two categories evolve separately along the redshift in this assumed function, there is a discontinuity point in the column density distribution as seen in Figure 1 (a). More recent work by Meiksin (2006) also adopted such a separate treatment of the LAF and LLSs.

Our previous work, Inoue & Iwata (2008) (hereafter II08), assumed the following function:

$$\frac{\partial^2 n}{\partial z \partial N_{\rm HI}} = f(z) g(N_{\rm HI}) \,, \tag{3}$$

where $f(z)$ and $g(N_{\rm HI})$ are the distribution functions in z and $N_{\rm HI}$ spaces, respectively. The spirit of this formulation is a universal column density distribution in any z and a common redshift evolution for all absorbers independent of $N_{\rm HI}$, producing no discontinuity in the column density distribution (see Fig. 1 [b]). II08 assumed a double power-law of $N_{\rm HI}$ for $g(N_{\rm HI})$ and a triple power-law of $(1+z)$ for $f(z)$.

As an extension of the II08 formalism, we here introduce the following function composed of two components named as the LAF and DLA components, respectively:

$$\frac{\partial^2 n}{\partial z \partial N_{\rm HI}} = f_{\rm LAF}(z) g_{\rm LAF}(N_{\rm HI}) + f_{\rm DLA}(z) g_{\rm DLA}(N_{\rm HI}) \,. \tag{4}$$

This is motivated by recent observations of the absorbers' statistics, especially the discovery of almost no evolution of the DLA encounter probability per unit 'absorption length' (Prochaska & Wolfe 2009) and the new measurements of the mean-free-path of the Lyman limit photons (Prochaska et al. 2009; O'Meara et al. 2013; Fumagalli et al. 2013; Worseck et al. 2014). We have found that it is very difficult to reproduce all the observed statistics simultaneously with the II08 formulation, i.e. a single component model. On the other hand, the two component model newly introduced in this paper can reproduce all the observations very well as shown in the following sections. Note that the two components both have all categories of absorbers as described below but one dominates the other in the column density range which the name indicates. The two components both significantly contribute to LLSs. We also note that the formulation in this paper is not the unique solution but an example description reproducing all the observational statistics. In this sense, we do not determine the parameters in the functions by any statistical test but do just by eye in comparisons with observations below. Nevertheless, we may suggest

[1] In fact, the absorbers are correlated with each other and even with the observing distant object (e.g., Slosar et al. 2011; Rudie et al. 2013; Prochaska et al. 2014). However, we reserve constructing a model with such a correlation for future work as done in the literature.

Table 1. Parameters for the distribution function of intergalactic absorbers assumed in this paper.

Common							
Parameter	$\log_{10}(N_{\rm l}/{\rm cm}^{-2})$	$\log_{10}(N_{\rm u}/{\rm cm}^{-2})$	$\log_{10}(N_{\rm c}/{\rm cm}^{-2})$	$\langle b/{\rm km\ s}^{-1}\rangle$			
Value	12	23	21	28			
LAF component							
Parameter	$\mathcal{A}_{\rm LAF}$	$\beta_{\rm LAF}$	$z_{\rm LAF,1}$	$z_{\rm LAF,2}$	$\gamma_{\rm LAF,1}$	$\gamma_{\rm LAF,2}$	$\gamma_{\rm LAF,3}$
Value	500	1.7	1.2	4.7	0.2	2.7	4.5
DLA component							
Parameter	$\mathcal{A}_{\rm DLA}$	$\beta_{\rm DLA}$	$z_{\rm DLA,1}$	—	$\gamma_{\rm DLA,1}$	$\gamma_{\rm DLA,2}$	—
Value	1.1	0.9	2.0	—	1.0	2.0	—

that the success of this separate treatment of the LAF and DLAs means different origins of the two categories. That is, the LAF traces diffuse filaments of the cosmic web not associated with halos and galaxies yet (e.g., Cen et al. 1994), but DLAs are associated with materials in halos and galaxies (e.g., Haehnelt et al. 1998).

In this paper, we assume a column density distribution function matching with the observed shape but still integrable analytically. One example of such functions is as follows:

$$g_i(N_{\rm HI}) = B_i {N_{\rm HI}}^{-\beta_i} e^{-N_{\rm HI}/N_{\rm c}}\,, \tag{5}$$

where the subscript $i =$ LAF or DLA, β_i is the power-law index for each component, $N_{\rm c}$ is the cut-off column density assumed to be common to the two components, and B_i is the normalization determined by $\int_{N_{\rm l}}^{N_{\rm u}} g_i(N_{\rm HI})dN_{\rm HI} = 1$ with the boundaries of $N_{\rm l}$ and $N_{\rm u}$ which are also assumed to be common to the two components. Thus, each component has in fact all types of absorbers from the LAF to DLAs, but the LAF (or DLA) component negligibly contributes to the DLA (LAF) number density as shown in Figure 1 (c) and (d). We also note that the function g_i is still continuous outside of these boundaries and we integrate g_i from 0 to ∞ in equation (1). Some analytic integrations of this function are found in appendix.

The redshift distribution functions, $f_i(z)$, are assumed to be broken power-laws of $(1+z)$ as follows: for the LAF component,

$$f_{\rm LAF}(z) = \mathcal{A}_{\rm LAF} \begin{cases} \left(\frac{1+z}{1+z_{\rm LAF,1}}\right)^{\gamma_{\rm LAF,1}} & (z < z_{\rm LAF,1}) \\ \left(\frac{1+z}{1+z_{\rm LAF,1}}\right)^{\gamma_{\rm LAF,2}} & (z_{\rm LAF,1} \leqslant z < z_{\rm LAF,2}) \\ \left(\frac{1+z_{\rm LAF,2}}{1+z_{\rm LAF,1}}\right)^{\gamma_{\rm LAF,2}} \left(\frac{1+z}{1+z_{\rm LAF,2}}\right)^{\gamma_{\rm LAF,3}} & (z_{\rm LAF,2} \leqslant z) \end{cases}, \tag{6}$$

and for the DLA component,

$$f_{\rm DLA}(z) = \mathcal{A}_{\rm DLA} \begin{cases} \left(\frac{1+z}{1+z_{\rm DLA,1}}\right)^{\gamma_{\rm DLA,1}} & (z < z_{\rm DLA,1}) \\ \left(\frac{1+z}{1+z_{\rm DLA,1}}\right)^{\gamma_{\rm DLA,2}} & (z_{\rm DLA,1} \leqslant z) \end{cases}. \tag{7}$$

The normalization of each component $\mathcal{A}_i$, where $i =$ LAF or DLA, is the number of absorbers with the column density $N_{\rm l} \leqslant N_{\rm HI} \leqslant N_{\rm u}$ per unit redshift interval at the redshift $z_{i,1}$. Note that the normalization $\mathcal{A}_i$ would be different if we chose other sets of $N_{\rm l}$ and $N_{\rm u}$. The fiducial set of the parameters in the functions, f_i and g_i, is summarised in Table 1, which is obtained from comparisons with observations as shown in the following sections.

2.1 Column density distribution

First, we compare the column density distribution functions with observations. The observed column density distributions are normally described by the number of absorbers per unit column density $dN_{\rm HI}$ and per unit 'absorption length' dX (Bahcall & Peebles 1969):

$$\frac{\partial^2 n}{\partial X \partial N_{\rm HI}} = \frac{\partial^2 n}{\partial z \partial N_{\rm HI}} \frac{dz}{dX}\,, \tag{8}$$

where

$$dX = \frac{H_0}{H(z)}(1+z)^2 dz\,, \tag{9}$$

with the Hubble parameters H_0 at the current epoch and $H(z)$ at the redshift z. Figure 1 (d) shows a comparison of the three models, this work, II08, and M95, with the observations at $z \sim 2.5$ compiled from the literature. We see a good agreement between the observations and the models. However, there are differences among them if we look closely as discussed below.

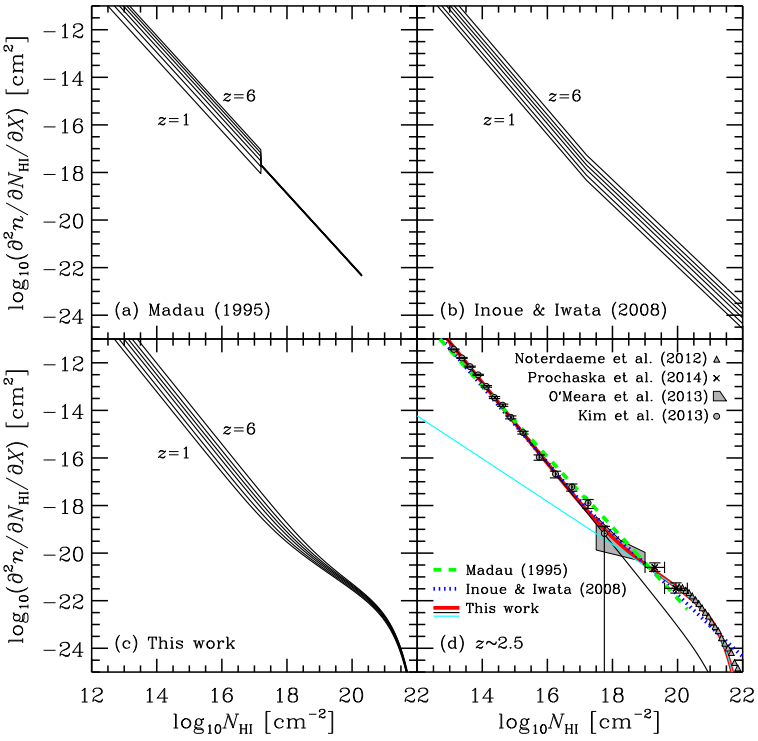

Figure 1. Number of the intergalactic absorbers per unit column density of neutral hydrogen ($N_{\rm HI}$) per unit absorption length (X) along an average line of sight as a function of the column density. (a) The redshift evolution of the functions in Madau (1995). (b) The same as (a) but for the model in Inoue & Iwata (2008). (c) The same as (a) but for the model of this work. (d) A comparison of the three models with the observational data at $z \sim 2.5$ taken from the literature: Kim et al. (2013) for LAF, O'Meara et al. (2013) for LLSs, Prochaska et al. (2014) for sub-DLAs (original data presented by O'Meara et al. 2007), and Noterdaeme et al. (2013) for DLAs. The solid, dotted, and dashed lines are models of this work, Inoue & Iwata (2008), and Madau (1995), respectively. The two thin solid lines show the LAF and DLA components in this work.

M95 adopted a single power-law index of -1.5 (e.g. Tytler 1987). However, recent observations suggest a break of the column density distribution around $N_{\rm HI} \sim 10^{17}$ cm^{-2} (Prochaska et al. 2005, 2010; O'Meara et al. 2013); the slope changes from a steeper at a lower column density to a shallower at a higher column density. The break column density is about the threshold of LLSs; the optical depth against the Lyman limit photon is about unity with this column density. Therefore, this break is probably caused by the transition between optically thin and thick against the ionizing background radiation (Corbelli et al. 2001; Corbelli & Bandiera 2002). Indeed, the latest cosmological radiation hydrodynamics simulations show that the self-shielding of the optically thick absorbers is the mechanism producing the break (Altay et al. 2011; Rahmati et al. 2013). On the other hand, M95 has the discontinuity at the column density as found in Figure 1 (a) owing to the different redshift evolutions of the LAF and LLSs.

II08 adopted a double power-law function in order to describe the break at $N_{\rm HI} \sim 10^{17}$ cm^{-2}. In fact, they assumed the break column density $N_{\rm HI} = 1.6 \times 10^{17}$ cm^{-2} at which the optical depth against the Lyman limit photon becomes unity. With this double power-law function for the column density distribution, II08 assumed a universal redshift evolution for all column densities. As a result, the number densities of LLSs and DLAs per unit absorption length monotonically increases with redshift as found in Figure 1 (b). However, recent observations suggest a much weaker evolution of DLAs (Prochaska et al. 2005; O'Meara et al. 2013) and the cosmological simulations successfully reproduce this weak evolution (Rahmati et al. 2013).

In this paper, we have assumed in equation (5) a power-law function with an exponential cut-off like the Schechter function. Such a functional shape has been already proposed by Prochaska et al. (2005) to describe the column density distribution of DLAs. As found at highest column densities in Figure 1 (d), this function reproduces the DLA distribution very well if we adopt a cut-off column density $N_{\rm c} \simeq 10^{21}$ cm^{-2}. With this functional shape, we successfully reproduce the weak evolution of the column density distribution of DLAs as shown in Figure 1 (c). This is partly due to a weaker redshift evolution in the DLA regime of this paper than II08 as discussed in Figure 2 below, but the constancy of the cut-off column density is also important. On the other hand, M95 also predicts almost no evolution of LLSs due to its weak redshift evolution for absorbers with the high column density (see eq. [2]). However, the M95 model does not have any DLAs.

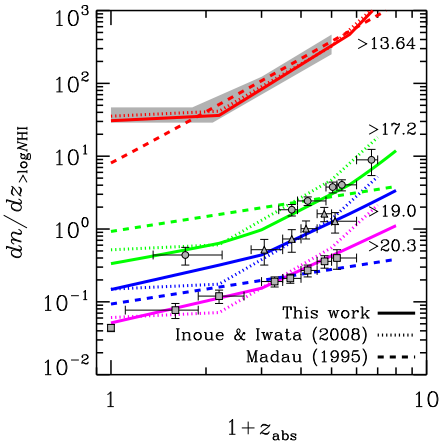

Figure 2. Number of the intergalactic absorbers per unit redshift along an average line of sight as a function of the absorbers' redshift. The shaded area is the observed range for absorbers with $\log_{10}(N_{\mathrm{HI}}/\mathrm{cm}^{-2}) > 13.6$ (LAF) taken from Weymann et al. (1998), Kim et al. (2001) and Janknecht et al. (2006). The filled circles, triangles and squares are the observed data of absorbers with $\log_{10}(N_{\mathrm{HI}}/\mathrm{cm}^{-2}) > 17.2$ (LLS) taken from Songaila & Cowie (2010), > 19.0 (sub-DLA) taken from Péroux et al. (2005), and > 20.3 (DLA) taken from Rao et al. (2006), respectively. The solid, dotted, and dashed lines are the models of this work, Inoue & Iwata (2008), and Madau (1995). Note that Madau (1995) model does not have DLAs.

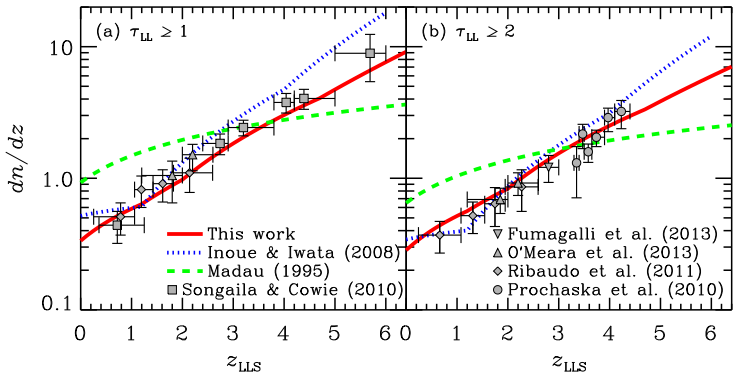

Figure 3. Number of LLSs per unit redshift along an average line of sight as a function of the LLSs' redshift: (a) the systems with the optical depth for hydrogen Lyman limit photons equal to or larger than unity, and (b) the systems with the optical depth equal to or larger than two. The squares, diamonds, triangles, upside-down triangles, and circles are the observed data taken from Songaila & Cowie (2010), Ribaudo et al. (2011), O'Meara et al. (2013), Fumagalli et al. (2013), and Prochaska et al. (2010), respectively. The solid, dotted, and dashed lines are the models of this work, Inoue & Iwata (2008), and Madau (1995), respectively.

2.2 Number density evolution

Next, we look into the number density evolution along the redshift. Figure 2 shows the comparison of the models with observations for four categories of absorbers depending on the column density: $\log_{10}(N_{\mathrm{HI}}/\mathrm{cm}^{-2}) > 13.64$ (LAF), > 17.2 (LLSs), > 19.0 (sub-DLAs or super-LLSs), and > 20.3 (DLAs). Figure 3 shows a close-up of LLSs' evolution.

M95 adopted a single power-law of $(1 + z)$. This fits well with the LAF number density evolution at $z > 1$, but it predicts too small number density relative to the observations at $z < 1$, where the observed number density is almost constant (Weymann et al. 1998). The break of the observed LAF number density evolution at $z \sim 1$ is probably caused by the sharp decline of the ionizing background radiation from the epoch to the present (e.g. Davé et al. 1999). The LLS number evolution of M95 is largely different from the observations in respect of the slope, while the absolute value matches the observations at $z \sim 3$. Furthermore, the M95 model has too small number of sub-DLAs and does not have any DLAs.

II08 adopted a twice-broken power-law for the redshift evolution. The first break is set at $z \sim 1$ to describe the bent of the LAF number evolution and the second break is set at $z \sim 4$ to reproduce a rapid increase of the Lyα optical depth toward high-z (see the next section). The same function was assumed for all absorber categories in II08. It is still compatible with the observed LLS and sub-DLA evolutions, but the agreement becomes marginal for DLAs.

In this paper, we adopt two different evolutions for the LAF and DLA components. As found in Figure 2, this new description shows the best agreement with the observations for all absorber categories. Figure 3 shows that the new model

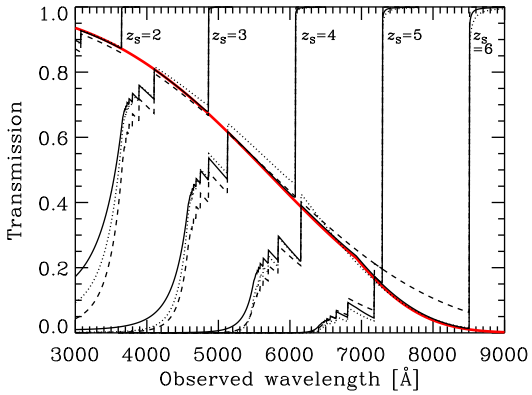

Figure 4. Mean transmission functions for sources at $z_S = 2$ to 6. The solid, dotted, and dashed lines are the models of this work, Inoue & Iwata (2008), and Madau (1995), respectively. The thick solid line is an analytic approximation for Lyα transmission given by equation (19) for the model of this work.

matches with observations better than the II08 model. In particular, the new model tends to have a smaller number of LLSs than II08. This point is essential to reproduce the observed mean-free-path for ionizing photons as discussed in section 3.2.

3 MEAN TRANSMISSION FUNCTION

With the distribution function of the intergalactic absorbers described in the previous section, we can integrate equation (1) numerically and obtain the mean transmission function of the IGM. In the integration, we treat the neutral hydrogen cross section $\sigma^{\rm HI}_{\lambda_{\rm abs}}$ as follows; we adopt the interpolation formula given by Osterbrock (1989) for the photoionization cross section. We also adopt the oscillator strengths and the damping constants taken from Wiese et al. (1966) and the analytic formula of the Voigt profile given by Tepper-García (2006) for the Lyman series cross sections. The mean Doppler velocity is assumed to be $\langle b\rangle = 28$ km s^{-1} obtained from the b distribution function proposed by Hui & Rutledge (1999) and its parameter $b_\sigma = 23$ km s^{-1} measured by Janknecht et al. (2006) for this work (see Table 1) and II08. On the other hand, we adopt $\langle b\rangle = 35$ km s^{-1} for M95 according to the original assumption. In the integration of equation (1), we should set the redshift step, Δz, to be fine enough to resolve the narrow width of the Lyman series lines. We adopt $\Delta z = 5\times10^{-5}$ and have confirmed the convergence of the calculations.

Figure 4 shows the mean transmission functions obtained. The three models are very similar but some differences are recognised if we look at them in detail. In the regime of the Lyman series transmission for $z_S \leqslant 4$, the II08 model is the highest, the M95 model is the lowest, and the new model of this paper is middle. On the other hand, the M95 model predicts the highest transmission for $z_S \geqslant 5$. However, the difference is small, except for the case of $z_S = 6$. This small difference comes from the small difference of the number density of the LAF, which mainly produces the Lyman series absorption, among the three models as seen in Figure 2. The deviation of the M95 model found in the wavelength between Lyα and Lyβ for $z_S = 6$ is due to the lack of a rapid increase of the LAF number density at high-z which are adopted in the other two models. This point will be discussed again in Figure 5 below.

In the Lyman continuum regime, the new model predicts the highest transmission, while the M95 model is the lowest for $z_S \leqslant 4$ and the II08 model is the lowest for $z_S \geqslant 5$ (but it is difficult to see in Fig. 4). Given that LLSs are mainly responsible for the Lyman continuum absorption, this difference is caused by the difference of the number density of LLSs. Indeed, M95 has the largest density of LLSs at $z_{\rm LLS} < 3$ and the LLS density of II08 becomes the largest at $z_{\rm LLS} > 3$ (see Fig. 3). In the next two subsections, we compare the model transmissions with the observations more in detail in terms of the Lyα transmission and the mean-free-path for ionizing photons.

3.1 Lyα transmission

The spectrum between Lyα and Lyβ lines in the source rest-frame is absorbed by the Lyα transition of the neutral hydrogen in the IGM. This is called the Lyα depression (DA). Here we compare the three models discussed in this paper with the measurements of 1−DA, i.e. Lyα transmission (T_α), in Figure 5. M95 presented an analytic formula for the mean optical depth which corresponds to the transmission as $T_\alpha = \exp\left[-3.6\times10^{-3}(1+z_\alpha)^{3.46}\right]$, where $z_\alpha = \lambda_{\rm obs}/\lambda_\alpha - 1$ is the redshift of absorbers and the Lyα wavelength $\lambda_\alpha = 1215.67$ Å. This formula is shown by the dashed line in Figure 5. We have confirmed this formula from the mean transmission function which we obtained from the integration of equation (1) with the M95

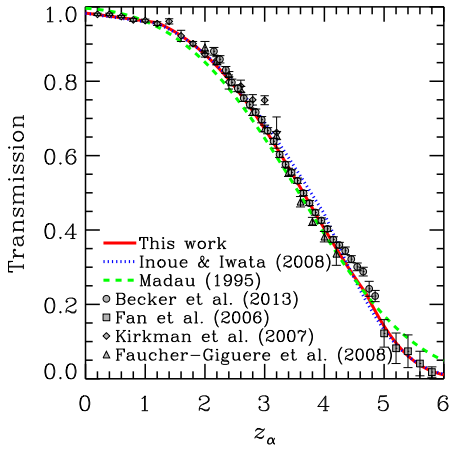

Figure 5. Lyα transmission as a function of the redshift of Lyα line. The triangles, diamonds, squares, and circles are the observed data taken from Fauche-Giguere et al. (2008), Kirkman et al. (2007), Fan et al. (2006), and Becker et al. (2013), respectively. The solid, dotted, and dashed lines are the models of this work, Inoue & Iwata (2008), and Madau (1995), respectively.

distribution function (eq. [2]).[2] We derive analytic formulae of T_α from the mean transmission functions of the II08 model and our new model which are shown by the dotted and the solid lines in Figure 5, respectively. The derivation is given in section 4 below. We find that all the three models excellently agree with the observations. Among them, the new model presented in this paper seems the best. In fact, the parameters for the LAF number density evolution along the redshift of the new model (eq. [6]) were chosen so as to match the observed T_α. However, the agreement is not perfect at $z \simeq 4.6$ where the observed data deviates upwards from the model. Although we found a better agreement with the data if we adopted a triple-break model instead of the double-break as equation (6), we avoid it to keep the model as simple as possible. If further observations emphasise the deviation, we should update the model again in the future. On the other hand, the M95 model predicts slightly smaller T_α at $1 < z < 4$ and larger at other redshifts than the observed data. In particular, the M95 model deviates from the observations at $z > 5$ because it does not have a rapid increase of the LAF number density towards the epoch of the reionization found in the last decade (e.g. Fan et al. 2006).

3.2 Mean-free-path of ionizing photons

Prochaska et al. (2009) (hereafter PWO) proposed a new method for measuring the mean-free-path in the IGM for ionizing photons directly in a composite spectrum of QSOs. Here we follow the method updated by O'Meara et al. (2013) (see also Fumagalli et al. 2013; Worseck et al. 2014). Suppose a source at the redshift $z_{\rm S}$ emitting an ionizing photon of the wavelength $\lambda_{\rm S} < \lambda_{\rm L}$, where the Lyman limit wavelength $\lambda_{\rm L} = 911.8$ Å (Cox 2000). The wavelength of the photon is redshifted cosmologically as it travels through the IGM. We suppose then that it becomes $\lambda_{\rm L}$ at the redshift $z_{\rm L}$. Namely, $\lambda_{\rm L}(1+z_{\rm L}) = \lambda_{\rm S}(1+z_{\rm S})$. The optical depth between $z_{\rm S}$ and $z_{\rm L}$ along the light path can be expressed as (O'Meara et al. 2013)[3]

$$\tau(z_{\rm L}, z_{\rm S}) = \int_{z_{\rm L}}^{z_{\rm S}} \kappa_{\rm L}(z) \left(\frac{1+z}{1+z_{\rm L}}\right)^{-2.75} \left|\frac{dl}{dz}\right| dz\,, \tag{10}$$

where $\kappa_{\rm L}$ is the IGM opacity for ionizing photons and $|dl/dz|$ is the proper length element per redshift. The index -2.75 comes from an approximate cross section of hydrogen atom for ionizing photons (O'Meara et al. 2013). Assuming $\kappa_{\rm L}(z) = \kappa_{\rm L,S}(1+z/1+z_{\rm S})^\gamma$ and $|dl/dz| \approx (c/H_0)\Omega_{\rm M}^{-1/2}(1+z)^{-3/2}$, we obtain

[2] There is a small difference ($< 10\%$) between the M95 T_α formula and that obtained from our numerical integration of equation (1). This is probably because the M95 formula was obtained from another distribution function based on the equivalent width, not based on the column density which we adopted in this paper.

[3] PWO and O'Meara et al. (2013) started from the following definition similar to equation (1) but a different interval in the redshift integration:

$$\tau(z_{\rm L}, z_{\rm S}) = \int_{z_{\rm L}}^{z_{\rm S}} \int_0^\infty \frac{\partial^2 n}{\partial z \partial N_{\rm HI}} \left(1 - e^{-N_{\rm HI}\sigma_{\rm ph}(z)}\right) dN_{\rm HI} dz\,,$$

where $\sigma_{\rm ph}(z) = \sigma_{\rm L}(1+z/1+z_{\rm L})^\alpha$ with $\sigma_{\rm L}$ and α being the Lyman limit cross section of neutral hydrogen and the power-law index of the wavelength dependence of the cross section, respectively. Then, they introduced the opacity $\kappa_{\rm L}(z)$ approximately to express the column density integration. Although the exact expression of the column density integration for the absorbers' function assumed in this paper is found in the appendix, we keep their expression to compare their measurements with our calculations directly.

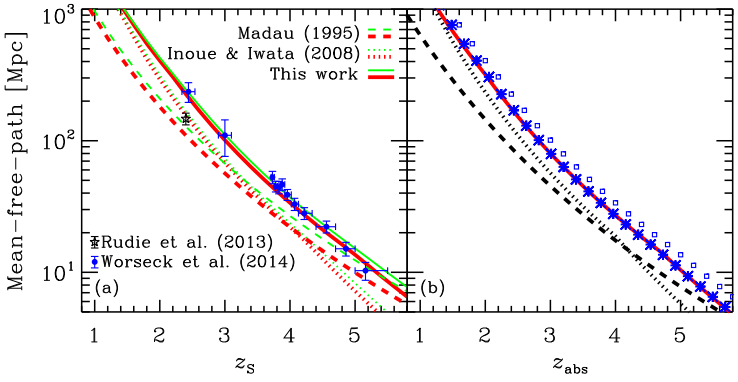

Figure 6. Mean-free-path for hydrogen Lyman limit photons as a function of (a) the source redshift and (b) the absorbers' redshift. (a) The circles with error-bars are the data taken from a compilation of Worseck et al. (2014). The solid, dotted, and dashed lines are the estimates obtained from the mean transmission functions of this paper, Inoue & Iwata (2008), and Madau (1995), respectively, by using the PWO method (eqs. [11] and [12]). The thick lines are the estimates within the wavelength range of 837 to 905 Å in the source rest-frame, which should be compared with the data at $z \geqslant 3$. The thin lines are that of 700 to 911 Å, which should be compared with the data at $z \sim 2.4$. (b) The solid, dotted, and dashed lines are the same as the panel (a), but based on equations (13) and (14). The small squares are the same result as the solid thick line in the panel (a) and these are moved to the asterisks by the conversion from the source redshift to the absorbers' redshift.

$$\tau(\lambda_S, z_S) \approx \kappa_{L,S} \frac{c(\lambda_S/\lambda_L)^{2.75}\{(\lambda_S/\lambda_L)^{\gamma-4.25}-1\}}{H_0\Omega_M^{1/2}(1+z_S)^{3/2}(4.25-\gamma)}\,, \tag{11}$$

where we have replaced $1+z_L$ by $(1+z_S)(\lambda_S/\lambda_L)$. Then, the mean-free-path at the redshift z_S is defined by (Prochaska et al. 2009; O'Meara et al. 2013; Fumagalli et al. 2013)

$$l_{mfp}(z_S) \equiv \frac{1}{\kappa_{L,S}}\,. \tag{12}$$

Prochaska et al. (2009), O'Meara et al. (2013), Fumagalli et al. (2013), Worseck et al. (2014) obtained the pivot opacities $\kappa_{L,S}$ by fitting their composite spectra of QSOs at various z_S with a function of $f_{\lambda_S}/f_L = \exp(-\tau[\lambda_S, z_S])$, where f_{λ_S} and f_L are the flux densities of the composite spectra at the wavelength λ_S and **at** the Lyman limit in the source rest-frame, respectively. Here we make a very similar fitting with the transmission functions numerically obtained in the previous subsection, T_{λ_S}, because we can express the composite spectrum as $f_{\lambda_S} = f^{int}_{\lambda_S} T_{\lambda_S}$, assuming an intrinsic QSO spectrum, $f^{int}_{\lambda_S}$. We here adopt the power-law spectrum reported by Telfer et al. (2002) for $f^{int}_{\lambda_S}$, while the change of the power-law index does not have a large impact because of the narrow wavelength range used for the fitting. The index γ in equation (11) is set to be 2.0 for the new model of this paper ($= \gamma_{DLA,2}$), 2.5 for the II08 model, and 0.68 for the M95 model, according to the LLS number density evolution at the most relevant redshift range. However, the choice does not affect the results very much (O'Meara et al. 2013; Fumagalli et al. 2013).

There is another definition of the mean-free-path, which may be more straightforward than that described above but more theoretical. Starting from equation (1), we can define the mean IGM opacity at the Lyman limit at z_{abs} as

$$\kappa_L(z_{abs}) \equiv \frac{d\langle\tau^{IGM}_{\lambda_L}(z_{abs})\rangle}{dz}\left|\frac{dz}{dl}\right| = \left|\frac{dz}{dl}\right|\int_0^\infty \frac{\partial^2 n}{\partial z \partial N_{HI}}(1-e^{-\sigma_L N_{HI}})dN_{HI}\,, \tag{13}$$

where we have replaced λ_{obs} by $\lambda_L(1+z_S)$ and z_S by z_{abs}. The latter replacement means that the opacity of equation (13) is one for the Lyman limit photon in the immediate proximity to the redshift emitted; $\lambda_{abs} = \lambda_L$. Note that σ_L is the photoionization cross section for the Lyman limit photon. We can integrate equation (13) numerically easily with the absorber distribution function assumed. Then, the mean-free-path is given by

$$l_{mfp}(z_{abs}) \equiv \frac{1}{\kappa_L(z_{abs})}\,. \tag{14}$$

Figure 6 shows the resultant mean-free-paths. In the panel (a), we show the comparison of the mean-free-path taken from Worseck et al. (2014) with the three models discussed in this paper. Their measurements are obtained from the fitting in the wavelength range of 837–905 Å for $z \sim 4$ (Prochaska et al. 2009), 700–911 Å for $z = 2.4$ (O'Meara et al. 2013), 830–905 Å for $z = 3$ (Fumagalli et al. 2013), and 850–910 Å for $z > 4.5$ (Worseck et al. 2014). These wavelength ranges are in the source rest-frame. We have made fittings of the mean transmission curves in the $z = 2.4$ and $z \sim 4$ wavelength ranges and obtained the mean-free-paths which are shown by the solid, dotted, and dashed lines in the panel (a). We find an excellent agreement between the new model and the observations. On the other hand, the II08 and M95 models predict shorter mean-free-paths than the observations. At this stage, these old models have been inconsistent with the observations.

There is another recent measurement of the mean-free-path at $z \approx 2.4$ by Rudie et al. (2013) which is a factor of 2 shorter than that by O'Meara et al. (2013). According to Prochaska et al. (2014), the effects of line-blending and clustering of strong absorption systems like LLSs may cause such a discrepancy. In this paper, we adopt the measurement by O'Meara et al. (2013) for $z \approx 2.4$ and just show the measurement by Rudie et al. (2013) in Figure 6 (a) for a comparison.

Figure 6 (b) shows the difference between the two definitions of the mean-free-path introduced above (eqs. [12] and [14]). The solid line is the mean-free-path calculated from equation (14), but the small squares are calculated from equation (12): the PWO method. We find a small displacement between the two. We consider its origin to be the difference of the redshifts; the displacement is horizontal not vertical. The PWO method (eq. [12]) measures the mean-free-path of the photons with the wavelength ≈ 870 Å at $z_{\rm S}$. But the wavelength of this photon is redshifted to the Lyman limit at $z_{\rm abs}$ at which equation (14) gives the mean-free-path. If we convert $z_{\rm S}$ in the PWO method into $z_{\rm abs}$, we obtain the asterisks and find an excellent agreements of the two mean-free-paths. Therefore, one should take care of the definition of the mean-free-path to compare a result with another.

4 NEW ANALYTIC MODEL

In this section, we derive a set of analytic approximation formulae for the mean transmission function numerically obtained with the new distribution function of absorbers. For an analytic integration of equation (1), we approximate Lyman series line cross section profiles to be a narrow rectangular shape. Then, we treat each line optical depth and the Lyman continuum optical depth occurring at an observed wavelength $\lambda_{\rm obs}$ separately. Namely,

$$\langle \tau^{\rm IGM}_{\lambda_{\rm obs}}(z_{\rm S}) \rangle \approx \tau^{\rm LAF}_{\rm LS}(\lambda_{\rm obs}, z_{\rm S}) + \tau^{\rm DLA}_{\rm LS}(\lambda_{\rm obs}, z_{\rm S}) + \tau^{\rm LAF}_{\rm LC}(\lambda_{\rm obs}, z_{\rm S}) + \tau^{\rm DLA}_{\rm LC}(\lambda_{\rm obs}, z_{\rm S})\,. \tag{15}$$

The Lyman series (LS) optical depths are given as

$$\tau^{i}_{\rm LS}(\lambda_{\rm obs}, z_{\rm S}) = \sum_j \tau^i_j(\lambda_{\rm obs}, z_{\rm S}) = \sum_j \int_0^{z_{\rm S}} f_i(z) I_{i,j}(z) dz\,, \tag{16}$$

where τ^i_j is the optical depth of jth line of Lyman series of i (LAF or DLA) component and $I_{i,j}$ is the integration of the column density function g_i for the jth line given by equations (A13) and (A14). Likewise, the Lyman continuum (LC) optical depths are given as

$$\tau^{i}_{\rm LC}(\lambda_{\rm obs}, z_{\rm S}) = \int_0^{z_{\rm S}} f_i(z) I_{i,{\rm LC}}(z) dz\,, \tag{17}$$

where $I_{i,{\rm LC}}(z)$ is the column density integral again given by equations (A13) and (A14). In the following subsections, we present analytic formulae of these optical depths.

4.1 Lyman series absorption

For the Lyman series absorption, let us assume a narrow rectangular shape of the cross section of the Lyman series lines approximately in the integration of equation (1). For example, the Lyα cross section is assumed to be $\sigma_\alpha(\lambda) = \sigma_{\alpha,0}$ for $\lambda_\alpha - \Delta\lambda/2 < \lambda < \lambda_\alpha + \Delta\lambda/2$ and 0 for otherwise, where $\sigma_{\alpha,0}$ is the cross section at the line center of the Lyα wavelength λ_α. The width $\Delta\lambda$ can be expressed as $(\delta b/c)\lambda_\alpha$ where δ is a numerical factor, b is the Doppler velocity, and c is the light speed in the vacuum. If we assume a Gaussian line profile and the cross section integrated over the wavelength from 0 to ∞ to be equal to $\sigma_{\alpha,0}\Delta\lambda$, we obtain $\delta = \sqrt{\pi}$. However, the DLA component may contribute to the optical depth especially of higher order Lyman series lines, and in this case, there may be a contribution from the damping wing to the cross section, so that a larger δ value may be favorable. We thus determine the values of δ from a comparison with the numerical integration later.

In the rectangular cross section approximation, the optical depth for the Lyα absorption at the observed wavelength $\lambda_{\rm obs} = \lambda_\alpha(1+z_\alpha)$ is produced by absorbers within a narrow redshift range $(1+z_\alpha) \pm \Delta(1+z_\alpha)/2$, where $\Delta(1+z_\alpha) \approx (1+z_\alpha)(\delta b/c)$ if we omit the term including $(\delta b/c)^2$. Then, the Lyα optical depth is independent of the source redshift $z_{\rm S}$ but just depends on the absorbers' redshift z_α. We express it as $\tau_\alpha(z_\alpha)$. For this Lyα optical depth, the contribution of the DLA component can be neglected. In this case, equation (1) becomes

$$\tau_\alpha(z_\alpha) \approx f_{\rm LAF}(z_\alpha)(1+z_\alpha)\left(\frac{\delta b}{c}\right)\int_0^\infty g_{\rm LAF}(N_{\rm HI})(1-e^{-\sigma_{\alpha,0}N_{\rm HI}})dN_{\rm HI}\,. \tag{18}$$

According to the analytic integration of the column density distribution presented in equation (A13), we obtain the Lyα optical depth as

$$\tau_\alpha(z_\alpha) \approx f_{\rm LAF}(z_\alpha)(1+z_\alpha)\left(\frac{\delta b}{c}\right)(\sigma_{\alpha,0}N_{\rm l})^{\beta_{\rm LAF}-1}\Gamma(2-\beta_{\rm LAF})\,, \tag{19}$$

where Γ is a Gamma function. Adopting $\delta = \sqrt{\pi}$ (i.e., a Gaussian line profile approximation), we find an excellent agreement with the numerical solution as shown in Figure 4. This indeed indicates that the Lyα transmission is determined almost only by the LAF component. For other Lyman series lines, we replace $\sigma_{\alpha,0}$ with $\sigma_{j,0}$ for the jth line, and then, the optical depth function for the jth line has the same functional shape as that of Lyα:

$$\tau_j^{\rm LAF}(z_j) \propto f_{\rm LAF}(z_j)(1+z_j)\,, \tag{20}$$

where $1+z_j = \lambda_{\rm obs}/\lambda_j$ with the wavelength of the jth line λ_j. Given the functional shape of $f_{\rm LAF}$ in equation (6) with the fiducial set of the parameters, we obtain, for $\lambda_j < \lambda_{\rm obs} < \lambda_j(1+z_{\rm S})$,

$$\tau_j^{\rm LAF}(\lambda_{\rm obs}) = \begin{cases} A_{j,1}^{\rm LAF}\left(\frac{\lambda_{\rm obs}}{\lambda_j}\right)^{1.2} & (\lambda_{\rm obs} < 2.2\lambda_j) \\ A_{j,2}^{\rm LAF}\left(\frac{\lambda_{\rm obs}}{\lambda_j}\right)^{3.7} & (2.2\lambda_j \leqslant \lambda_{\rm obs} < 5.7\lambda_j) \\ A_{j,3}^{\rm LAF}\left(\frac{\lambda_{\rm obs}}{\lambda_j}\right)^{5.5} & (5.7\lambda_j \leqslant \lambda_{\rm obs}) \end{cases}, \tag{21}$$

otherwise $\tau_j^{\rm LAF}(\lambda_{\rm obs}) = 0$. The coefficients $A_{j,k}^{\rm LAF}$ ($k = 1$, 2, and 3) calculated with $\delta = \sqrt{\pi}$ are summarised in Table 2 with the wavelength λ_j up to the 40th line considered in this paper.

Comparing this analytic model with the numerical integration, we find a slight difference between them at higher order lines. This is qualitatively because the contribution of the DLA component increases for higher order lines. Note that the DLA component in this paper still has absorbers in the LLS and even LAF column density regimes. Therefore, we also consider the contribution of the DLA component to the Lyman series line absorption. This contribution is also expressed by equation (20) but with the DLA number density function, $f_{\rm DLA}$. From the comparison with the numerical solution, we find a good fit if we set $\delta = 5.0$ for the DLA component. Likewise the LAF case, we express the analytic optical depth as, for $\lambda_j < \lambda_{\rm obs} < \lambda_j(1+z_{\rm S})$,

$$\tau_j^{\rm DLA}(\lambda_{\rm obs}) = \begin{cases} A_{j,1}^{\rm DLA}\left(\frac{\lambda_{\rm obs}}{\lambda_j}\right)^{2.0} & (\lambda_{\rm obs} < 3.0\lambda_j) \\ A_{j,2}^{\rm DLA}\left(\frac{\lambda_{\rm obs}}{\lambda_j}\right)^{3.0} & (\lambda_{\rm obs} \geqslant 3.0\lambda_j) \end{cases}, \tag{22}$$

otherwise $\tau_j^{\rm DLA}(\lambda_{\rm obs}) = 0$. Table 2 presents a list of the coefficients.

4.2 Lyman continuum absorption

Substituting equations (A13) and (A14) for the column density integral, $I_{i,{\rm LC}}(z)$, in equation (17), for the LAF and DLA components, respectively, we obtain the optical depths by the two components as

$$\tau_{\rm LC}^{\rm LAF}(\lambda_{\rm obs}, z_{\rm S}) \approx \Gamma(2-\beta_{\rm LAF})(N_{\rm l}\sigma_{\rm L})^{\beta_{\rm LAF}-1}\int_0^{z_{\rm S}} f_{\rm LAF}(z)\left(\frac{1+z_{\rm L}}{1+z}\right)^{\alpha(\beta_{\rm LAF}-1)} dz\,, \tag{23}$$

and

$$\tau_{\rm LC}^{\rm DLA}(\lambda_{\rm obs}, z_{\rm S}) \approx \frac{\Gamma(1-\beta_{\rm DLA})}{\Gamma(1-\beta_{\rm DLA}, N_{\rm l}/N_{\rm c})}\int_0^{z_{\rm S}} f_{\rm DLA}(z)\left\{1-(N_{\rm c}\sigma_{\rm L})^{\beta_{\rm DLA}-1}\left(\frac{1+z_{\rm L}}{1+z}\right)^{\alpha(\beta_{\rm DLA}-1)}\right\} dz\,, \tag{24}$$

These integrals can be reduced to the following formulae, when $\lambda_{\rm obs} > \lambda_{\rm L}$, if we adopt the fiducial set of the parameters and the photoionization cross section index $\alpha = 3$. For the LAF component, when $z_{\rm S} < 1.2$,

$$\tau_{\rm LC}^{\rm LAF}(\lambda_{\rm obs}, z_{\rm S}) \approx \begin{cases} 0.325\left[\left(\frac{\lambda_{\rm obs}}{\lambda_{\rm L}}\right)^{1.2} - (1+z_{\rm S})^{-0.9}\left(\frac{\lambda_{\rm obs}}{\lambda_{\rm L}}\right)^{2.1}\right] & (\lambda_{\rm obs} < \lambda_{\rm L}(1+z_{\rm S})) \\ 0 & (\lambda_{\rm obs} \geqslant \lambda_{\rm L}(1+z_{\rm S})) \end{cases}, \tag{25}$$

when $1.2 \leqslant z_{\rm S} < 4.7$,

$$\tau_{\rm LC}^{\rm LAF}(\lambda_{\rm obs}, z_{\rm S}) \approx \begin{cases} 2.55\times10^{-2}(1+z_{\rm S})^{1.6}\left(\frac{\lambda_{\rm obs}}{\lambda_{\rm L}}\right)^{2.1} + 0.325\left(\frac{\lambda_{\rm obs}}{\lambda_{\rm L}}\right)^{1.2} - 0.250\left(\frac{\lambda_{\rm obs}}{\lambda_{\rm L}}\right)^{2.1} & (\lambda_{\rm obs} < 2.2\lambda_{\rm L}) \\ 2.55\times10^{-2}\left[(1+z_{\rm S})^{1.6}\left(\frac{\lambda_{\rm obs}}{\lambda_{\rm L}}\right)^{2.1} - \left(\frac{\lambda_{\rm obs}}{\lambda_{\rm L}}\right)^{3.7}\right] & (2.2\lambda_{\rm L} \leqslant \lambda_{\rm obs} < \lambda_{\rm L}(1+z_{\rm S})) \\ 0 & (\lambda_{\rm obs} \geqslant \lambda_{\rm L}(1+z_{\rm S})) \end{cases}, \tag{26}$$

and when $z_{\rm S} \geqslant 4.7$,

$$\tau_{\rm LC}^{\rm LAF}(\lambda_{\rm obs}, z_{\rm S}) \approx \begin{cases} 5.22\times10^{-4}(1+z_{\rm S})^{3.4}\left(\frac{\lambda_{\rm obs}}{\lambda_{\rm L}}\right)^{2.1} + 0.325\left(\frac{\lambda_{\rm obs}}{\lambda_{\rm L}}\right)^{1.2} - 3.14\times10^{-2}\left(\frac{\lambda_{\rm obs}}{\lambda_{\rm L}}\right)^{2.1} & (\lambda_{\rm obs} < 2.2\lambda_{\rm L}) \\ 5.22\times10^{-4}(1+z_{\rm S})^{3.4}\left(\frac{\lambda_{\rm obs}}{\lambda_{\rm L}}\right)^{2.1} + 0.218\left(\frac{\lambda_{\rm obs}}{\lambda_{\rm L}}\right)^{2.1} - 2.55\times10^{-2}\left(\frac{\lambda_{\rm obs}}{\lambda_{\rm L}}\right)^{3.7} & (2.2\lambda_{\rm L} \leqslant \lambda_{\rm obs} < 5.7\lambda_{\rm L}) \\ 5.22\times10^{-4}\left[(1+z_{\rm S})^{3.4}\left(\frac{\lambda_{\rm obs}}{\lambda_{\rm L}}\right)^{2.1} - \left(\frac{\lambda_{\rm obs}}{\lambda_{\rm L}}\right)^{5.5}\right] & (5.7\lambda_{\rm L} \leqslant \lambda_{\rm obs} < \lambda_{\rm L}(1+z_{\rm S})) \\ 0 & (\lambda_{\rm obs} \geqslant \lambda_{\rm L}(1+z_{\rm S})) \end{cases}. \tag{27}$$

Table 2. Wavelengths and coefficients for Lyman series absorption.

j	λ_j (Å)	$A_{j,1}^{\rm LAF}$	$A_{j,2}^{\rm LAF}$	$A_{j,3}^{\rm LAF}$	$A_{j,1}^{\rm DLA}$	$A_{j,2}^{\rm DLA}$
2 (Lyα)	1215.67	1.690e-02	2.354e-03	1.026e-04	1.617e-04	5.390e-05
3 (Lyβ)	1025.72	4.692e-03	6.536e-04	2.849e-05	1.545e-04	5.151e-05
4 (Lyγ)	972.537	2.239e-03	3.119e-04	1.360e-05	1.498e-04	4.992e-05
5	949.743	1.319e-03	1.837e-04	8.010e-06	1.460e-04	4.868e-05
6	937.803	8.707e-04	1.213e-04	5.287e-06	1.429e-04	4.763e-05
7	930.748	6.178e-04	8.606e-05	3.752e-06	1.402e-04	4.672e-05
8	926.226	4.609e-04	6.421e-05	2.799e-06	1.377e-04	4.590e-05
9	923.150	3.569e-04	4.971e-05	2.167e-06	1.355e-04	4.516e-05
10	920.963	2.843e-04	3.960e-05	1.726e-06	1.335e-04	4.448e-05
11	919.352	2.318e-04	3.229e-05	1.407e-06	1.316e-04	4.385e-05
12	918.129	1.923e-04	2.679e-05	1.168e-06	1.298e-04	4.326e-05
13	917.181	1.622e-04	2.259e-05	9.847e-07	1.281e-04	4.271e-05
14	916.429	1.385e-04	1.929e-05	8.410e-07	1.265e-04	4.218e-05
15	915.824	1.196e-04	1.666e-05	7.263e-07	1.250e-04	4.168e-05
16	915.329	1.043e-04	1.453e-05	6.334e-07	1.236e-04	4.120e-05
17	914.919	9.174e-05	1.278e-05	5.571e-07	1.222e-04	4.075e-05
18	914.576	8.128e-05	1.132e-05	4.936e-07	1.209e-04	4.031e-05
19	914.286	7.251e-05	1.010e-05	4.403e-07	1.197e-04	3.989e-05
20	914.039	6.505e-05	9.062e-06	3.950e-07	1.185e-04	3.949e-05
21	913.826	5.868e-05	8.174e-06	3.563e-07	1.173e-04	3.910e-05
22	913.641	5.319e-05	7.409e-06	3.230e-07	1.162e-04	3.872e-05
23	913.480	4.843e-05	6.746e-06	2.941e-07	1.151e-04	3.836e-05
24	913.339	4.427e-05	6.167e-06	2.689e-07	1.140e-04	3.800e-05
25	913.215	4.063e-05	5.660e-06	2.467e-07	1.130e-04	3.766e-05
26	913.104	3.738e-05	5.207e-06	2.270e-07	1.120e-04	3.732e-05
27	913.006	3.454e-05	4.811e-06	2.097e-07	1.110e-04	3.700e-05
28	912.918	3.199e-05	4.456e-06	1.943e-07	1.101e-04	3.668e-05
29	912.839	2.971e-05	4.139e-06	1.804e-07	1.091e-04	3.637e-05
30	912.768	2.766e-05	3.853e-06	1.680e-07	1.082e-04	3.607e-05
31	912.703	2.582e-05	3.596e-06	1.568e-07	1.073e-04	3.578e-05
32	912.645	2.415e-05	3.364e-06	1.466e-07	1.065e-04	3.549e-05
33	912.592	2.263e-05	3.153e-06	1.375e-07	1.056e-04	3.521e-05
34	912.543	2.126e-05	2.961e-06	1.291e-07	1.048e-04	3.493e-05
35	912.499	2.000e-05	2.785e-06	1.214e-07	1.040e-04	3.466e-05
36	912.458	1.885e-05	2.625e-06	1.145e-07	1.032e-04	3.440e-05
37	912.420	1.779e-05	2.479e-06	1.080e-07	1.024e-04	3.414e-05
38	912.385	1.682e-05	2.343e-06	1.022e-07	1.017e-04	3.389e-05
39	912.353	1.593e-05	2.219e-06	9.673e-08	1.009e-04	3.364e-05
40	912.324	1.510e-05	2.103e-06	9.169e-08	1.002e-04	3.339e-05

For the DLA component, when $z_{\rm S} < 2.0$,

$$\tau_{\rm LC}^{\rm DLA}(\lambda_{\rm obs}, z_{\rm S}) \approx \begin{cases} 0.211(1+z_{\rm S})^{2.0} - 7.66\times10^{-2}(1+z_{\rm S})^{2.3}\left(\frac{\lambda_{\rm obs}}{\lambda_{\rm L}}\right)^{-0.3} - 0.135\left(\frac{\lambda_{\rm obs}}{\lambda_{\rm L}}\right)^{2.0} & (\lambda_{\rm obs} < \lambda_{\rm L}(1+z_{\rm S})) \\ 0 & (\lambda_{\rm obs} \geqslant \lambda_{\rm L}(1+z_{\rm S})) \end{cases}, \tag{28}$$

and when $z_{\rm S} \geqslant 2.0$,

$$\tau_{\rm LC}^{\rm DLA}(\lambda_{\rm obs}, z_{\rm S}) \approx \begin{cases} 0.634 + 4.70\times10^{-2}(1+z_{\rm S})^{3.0} - 1.78\times10^{-2}(1+z_{\rm S})^{3.3}\left(\frac{\lambda_{\rm obs}}{\lambda_{\rm L}}\right)^{-0.3} & \\ \quad - 0.135\left(\frac{\lambda_{\rm obs}}{\lambda_{\rm L}}\right)^{2.0} - 0.291\left(\frac{\lambda_{\rm obs}}{\lambda_{\rm L}}\right)^{-0.3} & (\lambda_{\rm obs} < 3.0\lambda_{\rm L}) \\ 4.70\times10^{-2}(1+z_{\rm S})^{3.0} - 1.78\times10^{-2}(1+z_{\rm S})^{3.3}\left(\frac{\lambda_{\rm obs}}{\lambda_{\rm L}}\right)^{-0.3} & \\ \quad - 2.92\times10^{-2}\left(\frac{\lambda_{\rm obs}}{\lambda_{\rm L}}\right)^{3.0} & (3.0\lambda_{\rm L} \leqslant \lambda_{\rm obs} < \lambda_{\rm L}(1+z_{\rm S})) \\ 0 & (\lambda_{\rm obs} \geqslant \lambda_{\rm L}(1+z_{\rm S})) \end{cases}. \tag{29}$$

Note that these formulae are correct when $\lambda_{\rm obs} > \lambda_{\rm L}$.

4.3 Validity of the analytic formulae

Let us confirm the validity of the approximate analytic formulae derived in the two subsections above. We compare the formulae with the numerical integration of equation (1). As a result, Figure 7 shows the difference of the two optical depths divided by the numerical one by a contour in the plane of the source redshift and the source rest-frame wavelength. We find that the differences are less than a few percent in a large area when the source redshift is larger than 0.5. In the case of $z_{\rm S} < 0.5$,

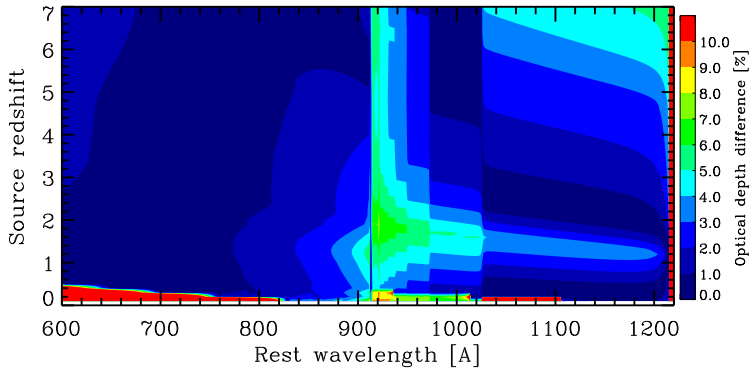

Figure 7. Fractional difference of the optical depths of the numerical integration of equation (1) and the approximate analytic formulae presented in sections 4.1 and 4.2. The formulae break down at the observed wavelength shorter than the Lyman limit. As a result, there appear parts where the difference exceeds 10% when the source redshift $z_{\rm S} < 0.52$.

the observed wavelength for some rest-frame wavelengths in the horizontal axis becomes shorter than the Lyman limit, and then, the formulae for the Lyman continuum absorption in section 4.2 become incorrect. As a result, the difference becomes $> 10\%$. For $z_{\rm S} > 0.5$, the difference tends to be relatively large for higher order Lyman series lines which the DLA component contributes to. Probably the rectangular shape approximation in the cross section is not very good for it. Nevertheless, the difference is still less than several percent and 8% at the most, ensuring the validity of the approximate formulae.

5 DISCUSSION

We here compare the attenuation magnitudes through some broad-band filters for the three models discussed in this paper, quantify the difference, and discuss the effect on the drop-out technique and the photometric redshift (hereafter photo-z) estimation.

Suppose the flux density observed through the IGM at the wavelength λ is expressed as $F_\lambda^{\rm obs} = F_\lambda^{\rm em} T_\lambda^{\rm IGM}$, where $F_\lambda^{\rm em}$ is the emitted flux density at the proximity of a cosmological object and $T_\lambda^{\rm IGM}$ is the IGM transmission. We assume a simple power law spectrum for $F_\lambda^{\rm em}$ with a rest-frame ultra-violet index $\beta_{\rm UV}$: $F_\lambda^{\rm em} \propto \lambda^{\beta_{\rm UV}}$. A band magnitude for using a photon-counting detector like CCDs is defined by $m = -2.5\log_{10} F + C_0$ with $F = \int (F_\nu t_\nu/h\nu)d\nu / \int (t_\nu/h\nu)d\nu = \int F_\lambda t_\lambda (\lambda/c)d\lambda / \int (t_\lambda/\lambda)d\lambda$, where $t_\nu = t_\lambda$ is the total (including the filter, detector, telescope and instrument optics, and atmosphere) efficiency of the band, and C_0 is the magnitude zero point. Thus, we can express the IGM attenuation through a band filter as

$$\Delta m_{\rm IGM} = -2.5\log_{10}\left(\frac{\int F_\lambda^{\rm obs} t_\lambda \lambda d\lambda}{\int F_\lambda^{\rm em} t_\lambda \lambda d\lambda}\right) = -2.5\log_{10}\left(\frac{\int \lambda^{\beta_{\rm UV}+1} T_\lambda^{\rm IGM} t_\lambda d\lambda}{\int \lambda^{\beta_{\rm UV}+1} t_\lambda d\lambda}\right). \quad (30)$$

Figure 8 shows the IGM attenuation magnitudes through 6 broad-band filters as a function of the source redshift in the case of $\beta_{\rm UV} = -2.0$, a flat continuum in F_ν unit usually observed in high-z star-forming galaxies (e.g., Shapley et al. 2003). We note here that the variation of $\beta_{\rm UV}$ from -3 to 0 (e.g., Bouwens et al. 2009) has a negligible effect on the attenuation magnitudes. The solid, dotted, and dashed lines are the models of this work, II08, and M95, respectively. The attenuation magnitudes shown in the figure are determined mainly by Lyα and Lyβ absorptions. Then, the difference seems to be small as expected from the small difference of the mean transmission curves among the three models shown in Figure 4. In fact, however, the vertical difference at a fixed source redshift reaches more than 1 mag between this work and the M95 model, while the horizontal difference is as small as about < 0.2, except for the deviation of the M95 model at $z_{\rm S} > 5.5$ owing to the lack of the rapid evolution of the Lyα optical depth included in the other two models. The thin (coloured) solid lines are the results from the analytic formulae for the new model presented in the previous section. We find an excellent agreement with the numerical integrations.

Although the horizontal difference at a certain amount of the attenuation magnitudes among the three models is small, there is a difference which would affect the drop-out technique and the photo-z estimation. The drop-out threshold is usually $\Delta m_{\rm IGM} \simeq 1$ mag. The source redshift reaching the threshold is different from the models. For example, the redshifts in the M95 model are about 0.2 smaller than those of this work at $z_{\rm S} \simeq 3$–4 but are about 0.1 larger at $z_{\rm S} \simeq 6$. These difference would result in systematically lower or higher photo-z solutions with the M95 model than with the new model of this paper. To check this expectation, we ran a photo-z code developed by Tanaka et al. (2013a,b) adopting two IGM models of this paper and M95. The sample is the galaxies with spectroscopic redshifts and photometry of VLT/VIMOS U, HST/ACS F435W, F606W, F775W, F814W, F850LP, HST/WFC3 F105W, F125W, F160W, VLT/ISAAC $K_{\rm s}$, Spitzer/IRAC *Ch1* and *Ch2* in the

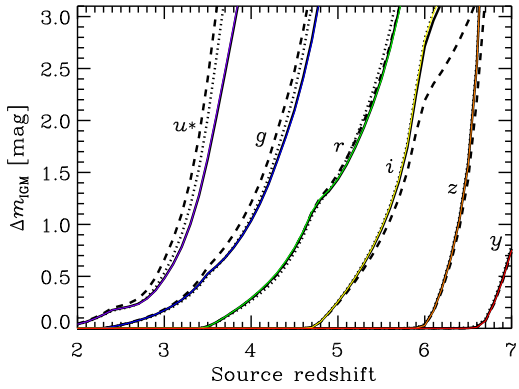

Figure 8. IGM attenuation magnitude through broad-band filters, the Canada-France-Hawaii Telescope/Mega-cam u^*, and the Subaru/Hyper Suprime-Cam g, r, i, z and y, as a function of the source redshift. The solid, dotted, and dashed lines are the models of this work, Inoue & Iwata (2008), and Madau (1995), respectively. The thin (coloured) solid lines are the cases using the analytic formulae for this work. The object spectrum with the ultra-violet spectral index $\beta_{\rm UV} = -2.0$ is assumed.

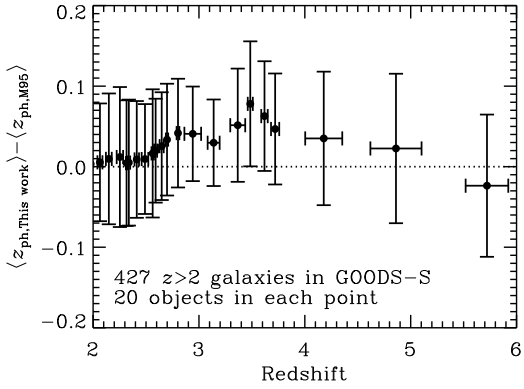

Figure 9. Difference of the means of the photometric redshift estimations assuming the IGM model of this work relative to those assuming the Madau (1995) model. The sample is 427 galaxies with spectroscopic redshift larger than 2 in the GOODS-S field and is divided into bins 20 objects each. Along the horizontal axis, the points and error-bars show the mean and the standard deviation of the spectroscopic redshifts in each bin. See the text for the vertical error-bars.

GOODS-S field (Guo et al. 2013). We collected spectroscopic redshifts from the literature (Le Fèvre et al. 2005; Mignoli et al. 2005; Vanzella et al. 2008; Popesso et al. 2009; Balestra et al. 2010) and cross-matched with the photometric objects within 1 arcsec. We use secure redshifts only in the analysis here. The photo-z code assumes the stellar population synthesis model by Bruzual & Charlot (2003) with solar and sub-solar metallicity models ($Z = 0.02$, 0.008, and 0.004), the Chabrier initial mass function between 0.1 and 100 $M_\odot$ (Chabrier 2003), exponentially declining star formation history, the Calzetti attenuation law (Calzetti et al. 2000), and the emission line model by Inoue (2011) with the Lyman continuum escape fraction of zero. The Lyα emission line is reduced by a factor of 0.1 to account for the attenuation through the interstellar medium of galaxies. The metallicity, age, exponential time-scale of the history, attenuation amount, and redshift are free parameters determined by a χ^2 minimization technique. We compare the photo-zs for the two IGM models in Figure 9. We divided the sample galaxies into bins 20 objects each and calculated the difference of the means of the photo-zs in each bin. The vertical error-bars are estimated by $\sqrt{\sum_i(\sigma^2_{\langle z_{{\rm ph},i}\rangle}/n + \delta^2_{z_{{\rm ph},i}}/n)}$, where i indicates the two IGM models (this work and M95), $\sigma_{\langle z_{{\rm ph},i}\rangle}$ is the standard deviation of the photo-zs in each bin, $\delta_{z_{{\rm ph},i}}$ is the mean of photo-z uncertainties of the sample galaxies in each bin, and $n = 20$ is the number of the sample galaxies in each bin. The first term is the standard error of the mean and the second term is the error in the mean propagated from the uncertainty of the individual photo-z. As found in Figure 9, the difference of the means of photo-zs is too small to be detected in the sample adopted, while we may find the expected trend of photo-zs for the new IGM model larger (or smaller) than those for the M95 model at $z \simeq 3$–5 ($z > 5.5$). The marginal difference of ≈ 0.05 at $z \simeq 3.5$ is much smaller than that expected from Figure 8. This is probably because we used not only the drop-out band but also all bands available in the photo-z estimation. As a result, the drop-out feature has a lower weight in the photo-z determination. However, all the available bands should be used in order to constrain intrinsic shapes of the spectral energy

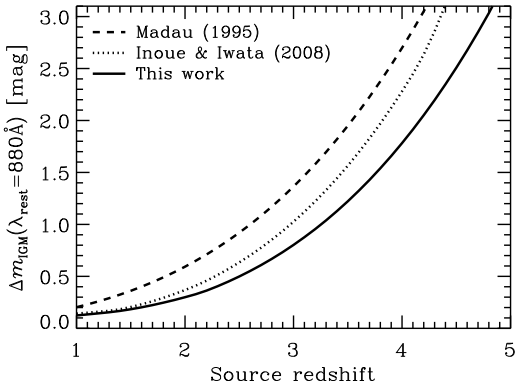

Figure 10. IGM attenuation magnitude at the rest-frame 880 Å as a function of the source redshift. The solid, dotted, and dashed lines are the models of this work, Inoue & Iwata (2008), and Madau (1995), respectively.

distribution below Lyα to characterize the IGM effect on photo-z. We would detect the IGM model difference securely if we had a ten times larger number of the sample galaxies at $z > 3$.

Finally, we examine the mean IGM attenuation magnitude at a Lyman continuum wavelength 880 Å in the source rest-frame as a function of the source redshift in Figure 10. This is motivated by studies for determining an important parameter controlling the cosmic reionization, the Lyman continuum escape fraction of galaxies (e.g., Inoue et al. 2005; Iwata et al. 2009). In these studies, we need to correct the IGM attenuation against the observed Lyman continuum of galaxies. As found in Figure 10, the difference among the three models discussed in this paper is significant; the new model predicts the least attenuation which is 0.5–1 mag smaller than the M95 model at $z_{\rm S} = 3$–4. This is consistent with those found in Figures 4 and 6. Note that this less attenuation against the Lyman continuum comes from the recent updates of the occurrence rate of LLSs discussed in section 2.2 and the measurements of the mean-free-path discussed in section 3.2. Therefore, using the M95 model causes a significant overcorrection of the observed Lyman continuum and results in an overestimation of the escape fraction. On the other hand, the Lyman continuum absorption is mainly caused by LLSs which are relatively rare to have on a line-of-sight. As a result, a large fluctuation of the attenuation amount among many lines-of-sight is expected. Therefore, a Monte-Carlo simulation is required to model the stochasticity as done in II08. This point would be investigated in our next work.

ACKNOWLEDGMENTS

We would like to thank the referee, J. Xavier Prochaska, for constructive comments useful to improve this manuscript. A.K.I. and I.S. are supported by JSPS KAKENHI Grant Number 23684010, I.I. is supported by JSPS KAKENHI Grant Number 24244018, and M.T. is supported by JSPS KAKENHI Grant Number 23740144.

REFERENCES

Altay, G., Theuns, T., Schaye, J., Crighton, N. H. M., Dalla Vecchia, C., 2011, ApJ, 737, L37
Bahcall, J. N., Peebles, P. J. E., 1969, ApJ, 156, L7
Balestra, I., Mainieri, V., Popesso, P., Dickinson, M., Nonino, M., Rosati, P., Teimoorinia, H., Vanzella, E., et al., 2010, A&A, 512, 12
Becker, G. D., Hewett, P. C., Worseck, G., Prochaska, J. X., 2013, MNRAS, 436, 1023
Bershady M. A., Charlton J. C., Geoffroy J. M., 1999, ApJ, 518, 103
Bouwens, R. J., Illingworth, G. D., Franx, M., Chary, R.-R., Meurer, G. R., Conselice, C. J., Ford, H., Giavalisco, M., van Dokkum, P., 2009, ApJ, 705, 936
Bruzual, G., Charlot, S., 2003, MNRAS, 344, 1000
Calzetti, D., Armus, L., Bohlin, R. C., Kinney, A. L., Koornneef, J., Storchi-Bergmann, T., 2000, ApJ, 533, 682
Cen, R., Miralda-Escudé, J., Ostriker, J. P., Rauch, M., 1994, ApJ, 437, L9
Chabrier, G., 2003, PASP, 115, 763
Corbelli, E., Salpeter, E. E., Bandiera, R., 2001, ApJ, 550, 26
Corbelli, E., Bandiera, R., 2002, ApJ, 567, 712
Cox, A. N., 2000, Allen's Astrophysical Quantities, 4th ed., AIP press, Springer, New York

Davé R., Hernquist L., Katz N., Weinberg D. H., 1999, ApJ, 511, 521
Fan, X., Strauss, M. A., Becker, R. H., White, R. L., Gunn, J. E., Knapp, G. R., Richards, G. T., Schneider, D. P., Brinkmann, J., Fukugita, M., 2006, AJ, 132, 117
Faucher-Giguère, C.-A., Prochaska, J. X., Lidz, A., Hernquist, L., Zaldarriaga, M., 2008, ApJ, 681, 831
Fumagalli, M., O'Meara, J. M., Prochaska, J. X., Worseck, G., 2013, ApJ, 775, 78
Gunn, J. E., Peterson, B. A., 1965, ApJ, 142, 1633
Guo, Y., Ferguson, H. C., Giavalisco, M., Barro, G., Willner, S. P., Ashby, M. L. N., Dahlen, T., Donley, J. L., et al., 2013, ApJS, 207, 24
Haehnelt, M. G., Steinmetx, M., Rauch, M., 1998, ApJ, 495, 647
Harrison, C. M., Meiksin, A., Stock, D., 2011, arXiv:1105.6208
Hui L., Rutledge R. E., 1999, ApJ, 517, 541
Inoue, A. K., Iwata, I., Deharveng, J.-M., Buat, V., Burgarella, D., 2005, A&A, 435, 471
Inoue, A. K., Iwata, I., 2008, MNRAS, 387, 1681 (II08)
Inoue, A. K., 2011, MNRAS, 415, 2920
Inoue, A. K., Kousai, K., Iwata, I., Matsuda, Y., Nakamura, E., Horie, M., Hayashino, T., Tapken, C., et al., 2011, MNRAS, 411, 2336
Iwata, I., Inoue, A. K., Matsuda, Y., Furusawa, H., Hayashino, T., Kousai, K., Akiyama, M., Yamada, T., et al., 2009, ApJ, 692, 1287
Janknecht, E., Reimers, D., Lopez, S., Tytler, D., 2006, A&A, 458, 427
Kim, T.-S., Cristiani S., D'Odorico S., 2001, A&A, 373, 757
Kim, T.-S., Partl, A. M., Carswell, R. F., Müller, V., 2013, A&A, 552, 77
Kirkman, D., Tytler, D., Lubin, D., Charlton, J., 2007, MNRAS, 376, 1227
Le Fèvre, O., Vettolani, G., Garilli, B., Tresse, L., Bottini, D., Le Brun, V., Maccagni, D., Picat, J. P., et al., 2005, A&A, 439, 845
Madau, P., 1995, ApJ, 441, 18 (M95)
Madau, P., Ferguson, H. C., Dickinson, M. E., Giavalisco, M., Steidel, C. C., Fruchter, A., 1996, MNRAS, 283, 1388
Meiksin, A., 2006, MNRAS, 365, 807
Mignoli M., et al., 2005, A&A, 437, 883
Møller, P., Jakobsen, P., 1990, A&A, 228, 299
O'Meara, J. M., Prochaska, J. X., Worseck, G., Chen, H.-W., Madau, P., 2013, ApJ, 765, 137
Osterbrock D. P., 1989, in Astrophysics of Gaseous Nebulae and Active Galactic Nuclei. University Science Books, Mill Valley, CA
Overzier, R., Lemson, G., Angulo, R. E., Bertin, E., Blaizot, J., Henriques, B. M. B., Marleau, G.-D., White, S. D. M., 2013, MNRAS, 428, 778
Paresce F., McKee C. F., Bowyer S., 1980, ApJ, 240, 387
Péroux, C., Dessauges-Zavadsky, M., D'Odorico, S., Kim, T.-S., McMahon, R. G., 2005, MNRAS, 363, 479
Popesso P., Dickinson, M., Nonino, M., Vanzella, E., Daddi, E., Fosbury, R. A. E., Kuntschner, H., Mainieri, V., et al., 2009, A&A, 494, 443
Prochaska, J. X., Herbert-Fort, S., Wolfe, A. M., 2005, ApJ, 635, 123
Prochaska, J. X., Wolfe, A. M., 2009, ApJ, 696, 1543
Prochaska, J. X., Worseck, G., O'Meara, J. M., 2009, ApJ, 705, L113 (PWO)
Prochaska, J. X., O'Meara, J. M., Worseck, G., 2010, ApJ, 718, 392
Prochaska, J. X., Madau, P., O'Meara, J. M., Fumagalli, M., 2014, MNRAS, 438, 476
Rahmati, A., Pawlik, A. H., Raičevič, Schaye, J., 2013, MNRAS, 430, 2427
Rao, S. M., Turnshek, D. A., Nestor, D. B., 2006, ApJ, 636, 610
Rauch, M., 1998, ARA&A, 36, 267
Ribaudo, J., Lehner, N., Howk, J. C., 2011, ApJ, 736, 42
Rudie, G. C., Steidel, C. C., Shapley, A. E., Pettini, M., 2013, ApJ, 769, 146
Shapley, A. E., Steidel, C. C., Pettini, M., Adelberger, K. L., 2003, ApJ, 588, 65
Slosar, A., Font-Ribera, A., Pieri, M. M., Rich, J., Le Goff, J.-M., Aubourg, R., Brinkmann, J., Busca, N., et al., 2011, Journal of Cosmology and Astroparticle Physics, 9, 1
Songaila, A., Cowie, L. L., 2010, ApJ, 721, 1448
Steidel, C. C., Pettini, M., Hamilton, D., 1995, AJ, 110, 2519
Tanaka, M., Finoguenov, A., Mirkazemi, M., Wilman, D. J., Mulchaey, J. S., Ueda, Y., Xue, Y., Brandt, W. N., Cappelluti, N., 2013a, PASJ, 65, 17
Tanaka, M., Toft, S., Marchesini, D., Zirm, A., De Breuck, C., Kodama, T., Koyama, Y., Kurk, J., Tanaka, I., 2013b, ApJ, 772, 113

Telfer, R. C., Zheng, W., Kriss, G. A., Davidsen, A. F., 2002, ApJ, 565, 773
Tepper-García T., 2006, MNRAS, 369, 2025
Tepper-García T., Fritze U., 2008, MNRAS, 383, 1671
Tytler, D., 1987, ApJ, 321, 49
Vanzella E., Cristiani, S., Dickinson, M., Giavalisco, M., Kuntschner, H., Haase, J., Nonino, M., Rosati, P., et al., 2008, A&A, 478, 83
Wiese, W. L., Smith, M. W., Glennon, B. M., 1966, Atomic Transition Probabilities, 1, US Department of Commerce, National Bureau of Standards, Washington
Weymann, R. J., Jannuzi, B. T., Lu, L., Bahcall, J. N., Bergeron, J., Boksenberg, A., Hartig, G. F., Kirhakos, S., et al., 1998, ApJ, 506, 1
Worseck, G., Prochaska, J. X., O'Meara, J. M., Becker, G. D., Ellison, S. L., Lopez, S., Meiksin, A., Ménard, B., et al., 2014, MNRAS, submitted (arXiv:1402.4154)
Yoshii, Y., Peterson, B. A., 1994, ApJ, 436, 551
Zuo, L., 1993, A&A, 278, 343

APPENDIX A: ANALYTIC INTEGRATION OF THE COLUMN DENSITY DISTRIBUTION

We have adopted in this paper a function similar to the Schechter function for the column density distribution of the IGM absorbers as

$$g_i(N_{\rm HI}) = B_i {N_{\rm HI}}^{-\beta_i} e^{-N_{\rm HI}/N_{\rm c}}\,, \tag{A1}$$

where i is either the LAF or DLA components. In this appendix, we present analytic functions of some integrals of g_i.

A1 Normalization factor

The normalization of the column density distribution is set to be

$$\int_{N_{\rm l}}^{N_{\rm u}} g_i(N_{\rm HI}) dN_{\rm HI} = 1\,. \tag{A2}$$

The normalization factor, B_i, is then given by

$${B_i}^{-1} = \int_{N_{\rm l}}^{N_{\rm u}} {N_{\rm HI}}^{-\beta_i} e^{-N_{\rm HI}/N_{\rm c}} dN_{\rm HI}\,. \tag{A3}$$

Substituting $x = N_{\rm HI}/N_{\rm c}$ for $N_{\rm HI}$, the integral is reduced to

$${B_i}^{-1} = {N_{\rm c}}^{1-\beta_i} \int_{x_{\rm l}}^{x_{\rm u}} x^{-\beta_i} e^{-x} dx\,, \tag{A4}$$

where $x_{\rm l} = N_{\rm l}/N_{\rm c}$ and $x_{\rm u} = N_{\rm u}/N_{\rm c}$. For the DLA component, we adopt $\beta_{\rm DLA} = 0.9$. In this case, we can obtain the normalization approximately as

$$B_{\rm DLA} \approx \frac{{N_{\rm c}}^{\beta_{\rm DLA}-1}}{\Gamma(1-\beta_{\rm DLA}, N_{\rm l}/N_{\rm c})}\,, \tag{A5}$$

where $\Gamma(1-\beta_{\rm DLA}, N_{\rm l}/N_{\rm c})$ is an incomplete Gamma function. We have omit the term $\Gamma(1-\beta_{\rm DLA}, N_{\rm u}/N_{\rm c})$. On the other hand, we adopt $\beta_{\rm LAF} = 1.7$ for the LAF component. By the method of integration by parts, equation (A4) can be reduced to

$${B_i}^{-1} = \left[\frac{{N_{\rm HI}}^{1-\beta_i} e^{-N_{\rm HI}/N_{\rm c}}}{1-\beta_i}\right]_{N_{\rm l}}^{N_{\rm u}} + \frac{{N_{\rm c}}^{1-\beta_i}}{1-\beta_i} \int_{x_{\rm l}}^{x_{\rm u}} x^{1-\beta_i} e^{-x} dx\,. \tag{A6}$$

Since the second term of the right hand side is negligible relative to the first term for the LAF component, we can obtain the normalization approximately as

$$B_{\rm LAF} \approx (\beta_{\rm LAF}-1) {N_{\rm l}}^{\beta_{\rm LAF}-1}\,, \tag{A7}$$

which is the same as the case of a single power-law distribution function.

A2 Integration for the mean optical depth

In order to perform the integration of equation (1) analytically, we should consider an approximation of the single absorber optical depth, $\tau_{\rm abs}$. If we approximate Lyman series line cross section profiles to be a narrow rectangular shape, we may treat each line optical depth and the Lyman continuum optical depth occurring at an observed wavelength $\lambda_{\rm obs}$ separately because different absorbers at different redshifts produce them (see also section 4). Then, equation (1) can be reduced to

$$\langle\tau^{\rm IGM}_{\lambda_{\rm obs}}(z_{\rm S})\rangle \approx \sum_i \sum_j \int_0^{z_{\rm S}} f_i(z) \int_0^\infty g_i(N_{\rm HI})(1-e^{-\tau_{{\rm abs},j}})dN_{\rm HI}dz\,, \tag{A8}$$

where i is either the LAF or DLA components and the optical depth for jth line (including the Lyman continuum absorption) by a single absorber can be expressed as $\tau_{{\rm abs},j} \approx N_{\rm HI}\sigma_j\eta_j(z)$ with σ_j being the jth line center cross section (and including the Lyman limit cross section $\sigma_{\rm L}$) and

$$\eta_j \approx \begin{cases} \left(\frac{1+z_{\rm L}}{1+z}\right)^\alpha & \text{(for Lyman continuum absorption)} \\ 1 & \text{(for } j\text{th Lyman series line absorption)} \end{cases}, \tag{A9}$$

where $1+z_{\rm L} = \lambda_{\rm obs}/\lambda_{\rm L}$. The power index $\alpha \approx 3$ (Osterbrock 1989). If we denote the column density integration as $I_{i,j}(z)$, it is

$$I_{i,j}(z) = \int_0^\infty B_i {N_{\rm HI}}^{-\beta_i} e^{-N_{\rm HI}/N_{\rm c}}\{1-e^{-N_{\rm HI}\sigma_j\eta_j(z)}\}dN_{\rm HI}\,. \tag{A10}$$

Substituting $\tau_j = N_{\rm HI}\sigma_j$ for $N_{\rm HI}$, equation (A10) can be reduced to

$$I_{i,j}(z) = B_i {\sigma_j}^{\beta_i-1} \int_0^\infty {\tau_j}^{-\beta_i} e^{-\tau_j/\tau_{\rm c}}\{1-e^{-\tau_j\eta_j(z)}\}d\tau_j \tag{A11}$$

where $\tau_{\rm c} = N_{\rm c}\sigma_j$. This is analytically integrable and we obtain for the case of $\beta_i \neq 1$

$$I_{i,j}(z) = B_i {\sigma_j}^{\beta_i-1}\Gamma(1-\beta_i){\tau_{\rm c}}^{1-\beta_i}\{1-[1+\tau_{\rm c}\eta(z)]^{\beta_i-1}\}\,, \tag{A12}$$

where $\Gamma(1-\beta_i) = \Gamma(2-\beta_i)/(1-\beta_i)$ is the Gamma function. Applying the normalization B_i obtained in appendix A1 and $\tau_{\rm c} \gg 1$ (and $\eta(z) \sim O(1)$), we finally obtain

$$I_{{\rm LAF},j}(z) \approx \Gamma(2-\beta_{\rm LAF})(N_{\rm l}\sigma_j\eta_j(z))^{\beta_{\rm LAF}-1}\,, \tag{A13}$$

for the LAF component and

$$I_{{\rm DLA},j}(z) \approx \frac{\Gamma(1-\beta_{\rm DLA})}{\Gamma(1-\beta_{\rm DLA}, N_{\rm l}/N_{\rm c})}\{1-(N_{\rm c}\sigma_j\eta_j)^{\beta_{\rm DLA}-1}\}\,, \tag{A14}$$

for the DLA component. Note that $\beta_{\rm LAF}-1 > 0$ but $\beta_{\rm DLA}-1 < 0$ for the fiducial set of the parameters in this paper (see Table 1).